THE JOURNAL OF PHYSICAL CHEMISTRY LETTERS
A JOURNAL OF THE AMERICAN CHEMICAL SOCIETY

pubs.acs.org/JPCL Letter

Squishing Skyrmions: Symmetry-Guided Dynamic Transformation of Polar Topologies Under Compression

Thomas Linker,[‖] Ken-ichi Nomura,[‖] Shogo Fukushima, Rajiv K. Kalia, Aravind Krishnamoorthy, Aiichiro Nakano,* Kohei Shimamura, Fuyuki Shimojo, and Priya Vashishta

Cite This: *J. Phys. Chem. Lett.* 2022, 13, 11335−11345 Read Online

ACCESS | Metrics & More | Article Recommendations | Supporting Information

ABSTRACT: Mechanical controllability of recently discovered topological defects (*e.g.*, skyrmions) in ferroelectric materials is of interest for the development of ultralow-power mechano-electronics that are protected against thermal noise. However, fundamental understanding is hindered by the "multiscale quantum challenge" to describe topological switching encompassing large spatiotemporal scales with quantum mechanical accuracy. Here, we overcome this challenge by developing a machine-learning-based multiscale simulation framework—a hybrid neural network quantum molecular dynamics (NNQMD) and molecular mechanics (MM) method. For nanostructures composed of $SrTiO_3$ and $PbTiO_3$, we find how the symmetry of mechanical loading essentially controls polar topological switching. We find under *symmetry-breaking* uniaxial compression a squishing-to-annihilation pathway versus formation of a topological composite named skyrmionium under *symmetry-preserving* isotropic compression. The distinct pathways are explained in terms of the underlying materials' elasticity and symmetry, as well as the Landau−Lifshitz−Kittel scaling law. Such rational control of ferroelectric topologies will likely facilitate exploration of the rich ferroelectric "topotronics" design space.

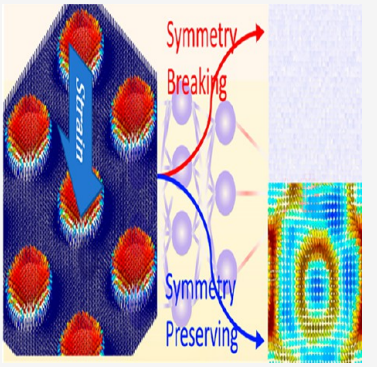

The formation of topological defects originally seen in particle physics such as skyrmions and merons[1−3] in the spin fields of ferromagnetic materials has garnered attention over the past two decades in the field of spintronics for the development of next generation information transfer and memory devices such as racetrack memory.[4] Recently, there has been growing effort to synthesize the electric analogue of these topological structures in ferroelectric materials, with the most prominent example being the synthesis of polar vortex states and skyrmion bubbles in paraelectric/ferroelectric $SrTiO_3$ (STO)/$PbTiO_3$ (PTO)-based nanosuperlattices.[5−10] The emergence of such topological structures in these heterostacks relies on a subtle balance of the strain gradients and polarization fields within the materials, which make them ideal for exploring low-power next generation devices, where optical, electrical, and mechanical manipulation of these strain and polarization fields switches structures that are topologically protected from thermal noise.[11,12] The majority of efforts in topological manipulation of these vortex and skyrmion states has focused on direct manipulation of the charge and polarization boundary conditions that give rise to skyrmion or vortex formation with static electric fields and ultrafast laser pulses, where topologically based switching has been experimentally and theoretically demonstrated.[6,7,9,13−15] While mechanical writing of ferroelectric polarization has been demonstrated,[16] direct mechanical manipulation of polar topological structures has been less explored, with primary efforts focused on strain engineering through modification of sample temperature, thickness, and substrate lattice mismatch.[17−20] In particular, little is known about the stability and phase changes of these topological defects to externally applied mechanical stresses. As a wide variety of loading modes and symmetries can be adopted for mechanical stimuli that can directly control strain fields within these nanostructures, it is most compelling to investigate the mechanical control of polar topology in order to establish a fundamental science of polar topological switching.

The rational mechanical control of polar topologies requires a fundamental understanding of the switching dynamics on picosecond to nanosecond time-scales on 10s to 100s of nanometers spatial scales.[11] In particular, it is essential to describe the dynamical response of the strain gradients to mechanical manipulation and the corresponding response of the polarization through static and dynamical flexoelectric effects.[21,22] In this regard, simulation methods utilizing atomistic level dynamics offer an appropriate theoretical framework; however, one of the main difficulties in exploring such phase changes atomistically is the prohibiting computational cost in modeling the polarization dynamics within the ferroelectric layer with quantum mechanical (QM) accuracy

Received: October 4, 2022
Accepted: November 16, 2022
Published: December 1, 2022

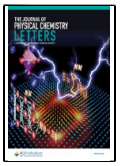

https://doi.org/10.1021/acs.jpclett.2c03029
J. Phys. Chem. Lett. 2022, 13, 11335−11345

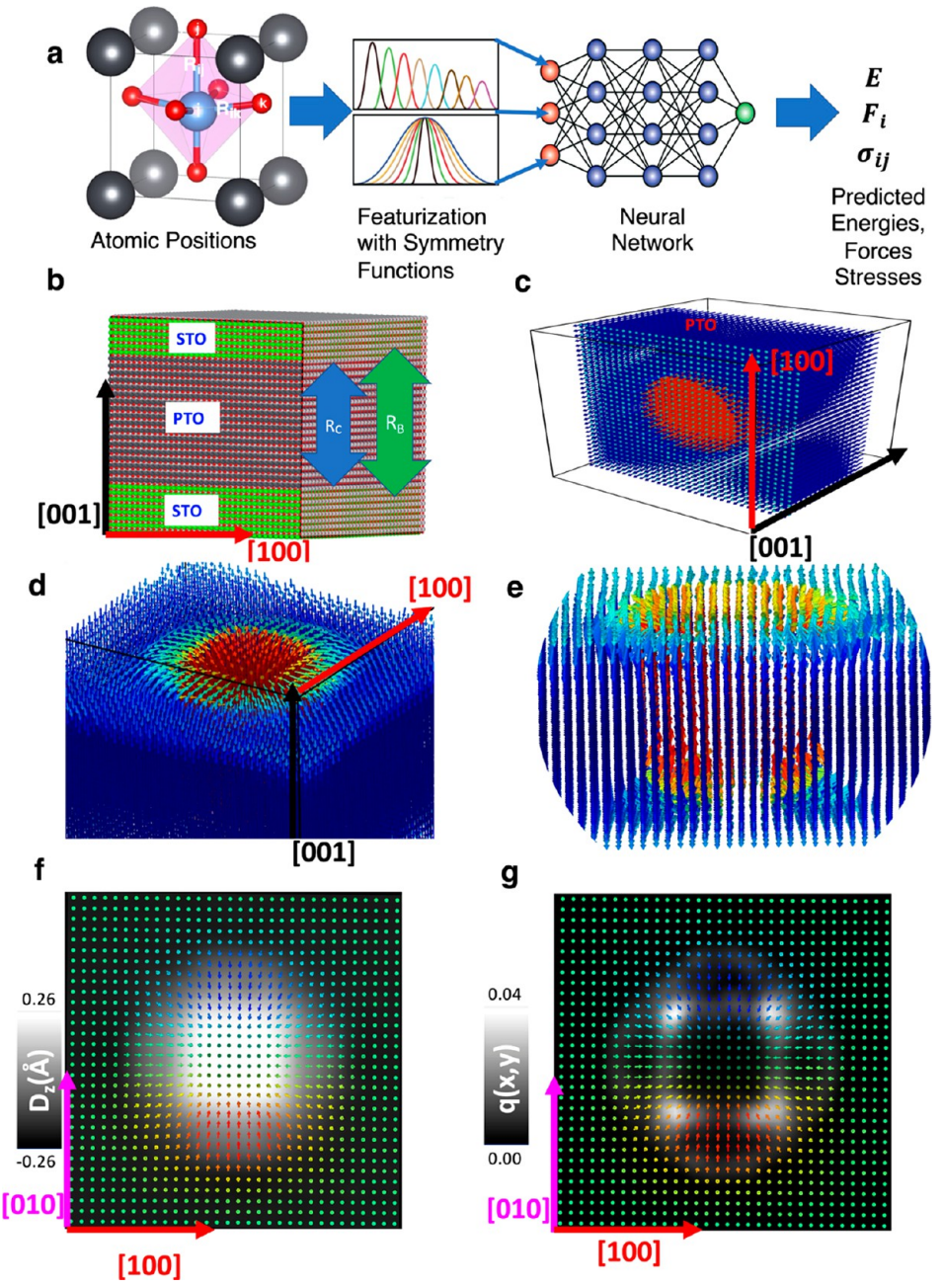

Figure 1. NN/MM model of STO/PTO superlattice ground-state structure. (a) NNQMD framework used for NN engine. Atomic coordinates are used to construct symmetry functions, which are fed into a neural network to predict energy, force, and stresses. (b) STO/PTO heterostack of 8 × 16 × 8 STO−PTO−STO unit cells with periodic boundary conditions. R_C and R_B represent the core and buffer radius to linearly mix the NNQMD and MM interactions at the boundary. (c) Represents the initial condition of the circular, oppositely polarized domain for the STO/PTO superlattice. (d) Top perspective view of STO/PTO skyrmion structure after relaxation. (e) Front perspective view of the skyrmion after relaxation. (f) (001) Plane view of polarization vectors with background density colored by interpolated [001] polar displacements of Ti atoms D_z. (g) (001) Plane view of polarization vectors with background colored by the topological charge density q.

on the spatiotemporal scales that these topologies emerge while maintaining the appropriate boundary conditions applied by the paraelectric layer. We addressed this challenge by employing a hybrid neural network[23] (NN) and molecular mechanics (MM) framework. Our framework draws from the hugely successful field of physics-informed machine learning (ML)[24] and expands it to physics−ML hybridization in the spirit of the celebrated multiscale simulation approach called QM/MM, which received the 2013 Nobel prize in chemistry.[25,26] In our NN/MM approach, a highly scalable neural network−quantum molecular dynamics (NNQMD)[15,27−29] force field is trained using *ab intio* molecular dynamics (MD) simulation data to accurately describe complex polarization dynamics within the ferroelectric layer, which, in turn, is embedded in a classical force field that correctly applies the essential strain and null polarization boundary conditions imposed by the paraelectric layer.

We applied the NN/MM framework to the study of mechanical manipulation of polar skyrmions in STO/PTO nanostructures under compressive strain. Individual MM and NN force fields were found to produce mechanical properties in good agreement for measured bulk STO and PTO, and the

https://doi.org/10.1021/acs.jpclett.2c03029
J. Phys. Chem. Lett. 2022, 13, 11335−11345

NN/MM model successfully describes the formation of polar skyrmions in STO/PTO nanostructures consistent with experimental and second principles and phase field simulations.[5,6] We examined the dynamics of these skyrmions in two strain modes with different symmetries: (1) uniaxial compression along the c polarization axis to mimic uniaxial loading along the polarization direction, and (2) isotropic compression to examine the effects of symmetry-preserving deformation of the skyrmion system.

Under the symmetry-breaking uniaxial compression, we found a squishing-to-annihilation phase transition marked by interfacial depolarization and rotation of the TiO_6 octahedra of PTO near the interface. We determined the depolarization at the interface to be due the compliance of the local c lattice constant to STO because of its stiffer C_{11} elastic constant, which eventually results in complete loss of polarization in the heterostack within picoseconds. Such mechanically induced rapid depolarization of the skyrmion structure could be of interest for pulsed power technologies through the force–electric effect.[30,31]

Under the symmetry-preserving isotropic compression, however, polarization reduction occurs, but annihilation is not seen. Skyrmion domains can become punctured, thereby leading to the formation of concentric skyrmions with opposite topological charges upon unloading of the pressure. The combination of the two oppositely charged skyrmions form a topological composite called skyrmionium,[32] which has been investigated in magnetic materials for next generation spintronics based devices[3,32−36] but not in ferroelectric materials. To the best of our knowledge, this is the first demonstration of skyrmion-to-skyrmionium "reaction" in ferroelectric materials. Moreover, we explain such "topological mechano-chemistry" on the basis of the well-known Landau–Lifshitz–Kittel scaling laws[37−39] for domain size versus thickness for ferroelectric and ferromagnetic domains. Namely, a decreasing sample thickness size increases the number of domains within the sample, which is consistent with the new domain walls creating the skyrmionium topology in the thinner structure. The observed skyrmion-to-skyrmionium phase transition offers a mechanical pathway to introducing more regions in the superlattice with local polarization curl and divergence, which are anticipated to enhance the macroscopic dielectric properties of the superlattice.[7]

In both strain modes, a phase transition occurs when the PTO lattice cannot maintain proper stress/strain gradients for the skyrmion because of the compression, but how this gradient is dissipated, and the corresponding dynamical response of the polarization, is fundamentally different depending on the symmetry of the applied strain modes. Overall, our machine-learning-based multiscale NN/MM simulations illuminate the complex interplay between the symmetry of the strain and polarization boundary conditions in the formation of topological defects while further demonstrating the ability of ferroelectric materials to materialize topological defects seen in the sister field of ferromagnetism.[11,12]

We explored the effects of mechanical manipulation of STO/PTO superlattices by first developing NN/MM force fields to describe their interactions. A diagram of the workflow for the neural network quantum molecular dynamics (NNQMD)[15,27−29] framework used for the NN engine to describe the dynamics in the PTO nanolayer within the NN/MM model is illustrated in Figure 1a. Atomic positions for a given lattice configuration from a density functional theory (DFT)-based quantum molecular dynamics (QMD) trajectory are used to compute highly scalable symmetry functions[40,41] that are then fed into a neural network, which is trained to predict the total energy of the quantum system computed from DFT. The NNQMD model was evaluated in terms of structure prediction with computation of the radial distribution functions and elastic properties with computation of the bulk modulus and elastic constant tensor. The NNQMD model was found to have good agreement with the DFT data and experiment. Details on the DFT training data generation, as well as model training and validation, are provided in the Methods section and Supporting Information section SI on NNQMD model training and testing. The appropriate boundary conditions of a paraelectric (zero) polarization field and strain applied by the cubic STO layer in an STO/PTO heterostack were applied by fitting an empirical interaction to reproduce the bulk modulus and cubic lattice constant for STO so as to describe its applied mechanical strain on the PTO layer correctly while maintaining a zero polarized field. The MM model was also found to have good agreement with the experiment in regard to the elastic modulus tensor. Details of the MM force field are provided in the Supporting Information section SII.

After validation of the prediction of desired bulk properties by the NNQMD model for PTO and by the MM model for STO, we examined if a combined NN/MM framework using the individually trained models could correctly describe polar skyrmion formation in the heterostack. We created a heterostack such that, along the [001] direction, 16 unit cells of PTO were stacked in between 8 unit cells of STO on each side with periodic boundary conditions for a total of 32 unit cells (16STO/16PTO), as illustrated in Figure 1b. The structure was expanded with 32 × 32 unit cells in the [100] × [010] directions. We handled the boundary between the STO/PTO region by employing a "core+buffer" approach commonly used in linear-scaling divide-and-conquer DFT simualtions.[42] From the center of the PTO region, a core distance R_C is defined for within which the forces and energies are determined by the NNQMD model. A second buffer distance R_B ($>R_C$) is defined for which interactions of atoms within $R_C < z < R_B$ are combined between the MM model for STO and the NNQMD model for PTO with linear support functions that form a partition of unity of the entire MD box. Beyond R_B, the interaction is described purely by STO MM. This approach is similar to linear interpolation approaches used in second-principles-based methods[5] and other buffer domain approaches in the rapidly emerging field of NN/MM force field development.[43] Further details on the boundary condition are provided in Supporting Information section SII.

The creation of the skyrmion was seeded by cutting out a 3.2 nm circle in the center of the PTO region superlattice and giving it opposite polarization, as illustrated in Figure 1c. A low-temperature simulation (10 K) in the canonical (NVT) ensemble was then performed to obtain the ground-state structure. Upon relaxation, we found the formation of skyrmions to be in line with what has been previously reported experimentally and with second-principles and phase-field simulation approaches.[5,6] A video of the skyrmion formation is provided in Supporting Video S1. The stability to thermal noise was tested up to 300 K with simulation in the NVT ensemble, for which the skyrmion was found to be stable. A video of thermalization is shown in Supporting Video S2. A top

https://doi.org/10.1021/acs.jpclett.2c03029
J. Phys. Chem. Lett. 2022, 13, 11335−11345

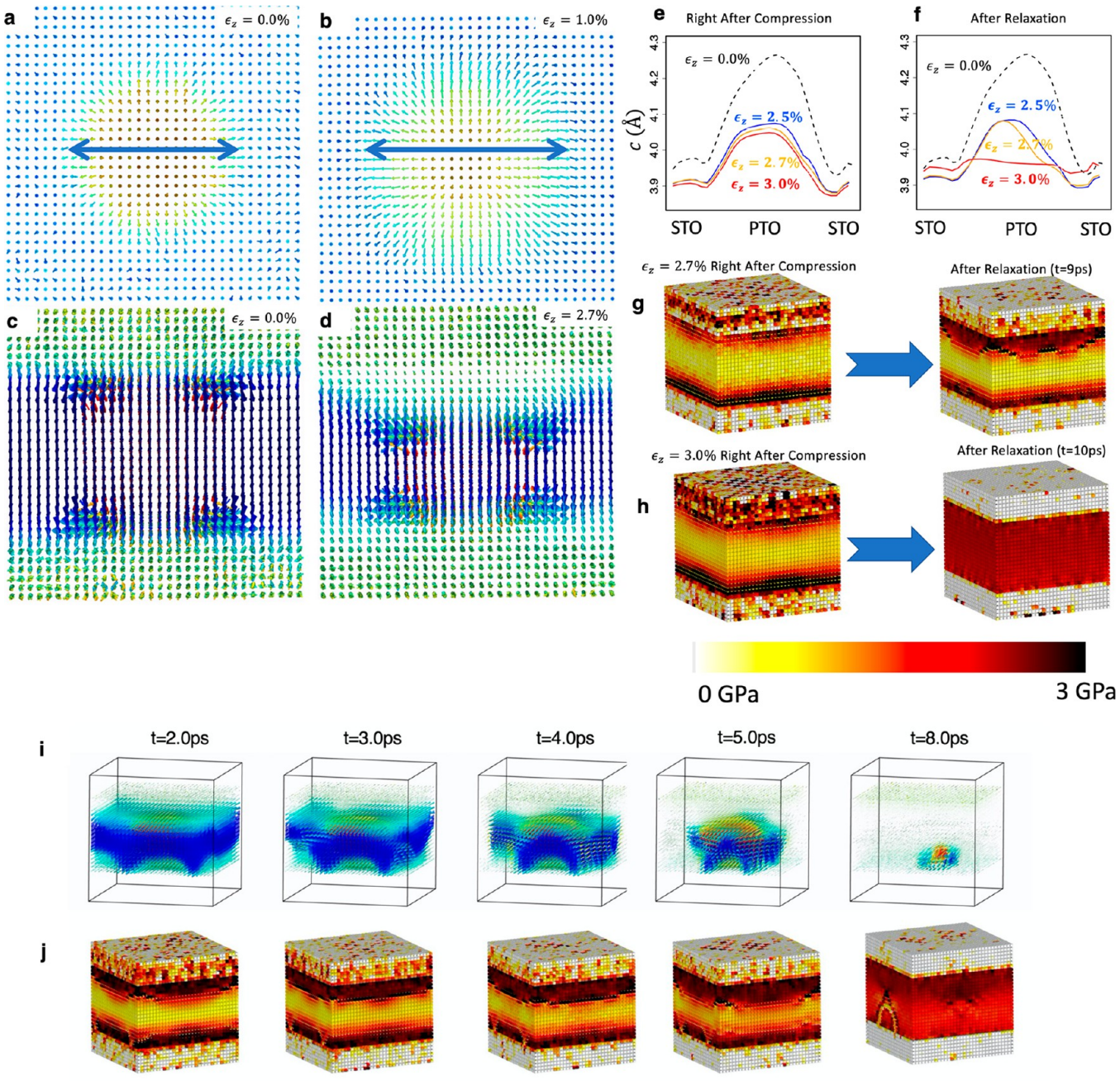

Figure 2. Skyrmion evolution under uniform compression. (a,b) Top slice of skyrmion polarization at 0.0% and 1.0% compression along [001]. Blue double arrows are given as a guide to the eye. (c,d) (010) Plane slice of skyrmion structure at 0.0% and 2.7% strain. (e,f) Local c lattice constant as a function of position along the interface after compression and evolution of the compressed structure. (g,h) Local pressure profiles for the heterostack after compression and evolution of the compressed structure. (i,j) Evolution of polarization and local pressure under 3.0% compression.

perspective view of the skyrmion texture is provided in Figure 1c, and a front perspective view highlighting the bubble texture is shown in Figure 1d. Figure 1e illustrates the smooth transition from negative to positive [001] Ti polar displacements in the (001) plane, which results in the formation of polarization along the [100] and [010] axes. We quantified the topological character of the skyrmion by computing the topological charge Q and density q in the (001) plane:

$$Q = \frac{1}{4\pi}\int\int q(x, y)\mathrm{d}x\mathrm{d}y = \frac{1}{4\pi}\int\int \boldsymbol{\mu}\cdot(\partial_x\mathbf{u} \times \partial_y\mathbf{u})\mathrm{d}x\mathrm{d}y \quad (1)$$

where $\mathbf{u}$ is the normalized dipole moment, and x and y correspond to the [100] and [010] directions. We found Q = 1, which is consistent with the formation of a skyrmion. The computation was performed on an interpolated grid using the method outlined in ref 44 to ensure an integer topological charge.

After validation of the NN/MM framework to describe the formation of skyrmion domains in an STO/PTO superlattice, we examined the dynamics of the domains under compression. PTO possesses a low-temperature tetragonal structure in the $P4mm$ space group (see Figure S2a) that is ferroelectric and a high-temperature paraelectric cubic phase belonging to the

https://doi.org/10.1021/acs.jpclett.2c03029
J. Phys. Chem. Lett. 2022, 13, 11335−11345

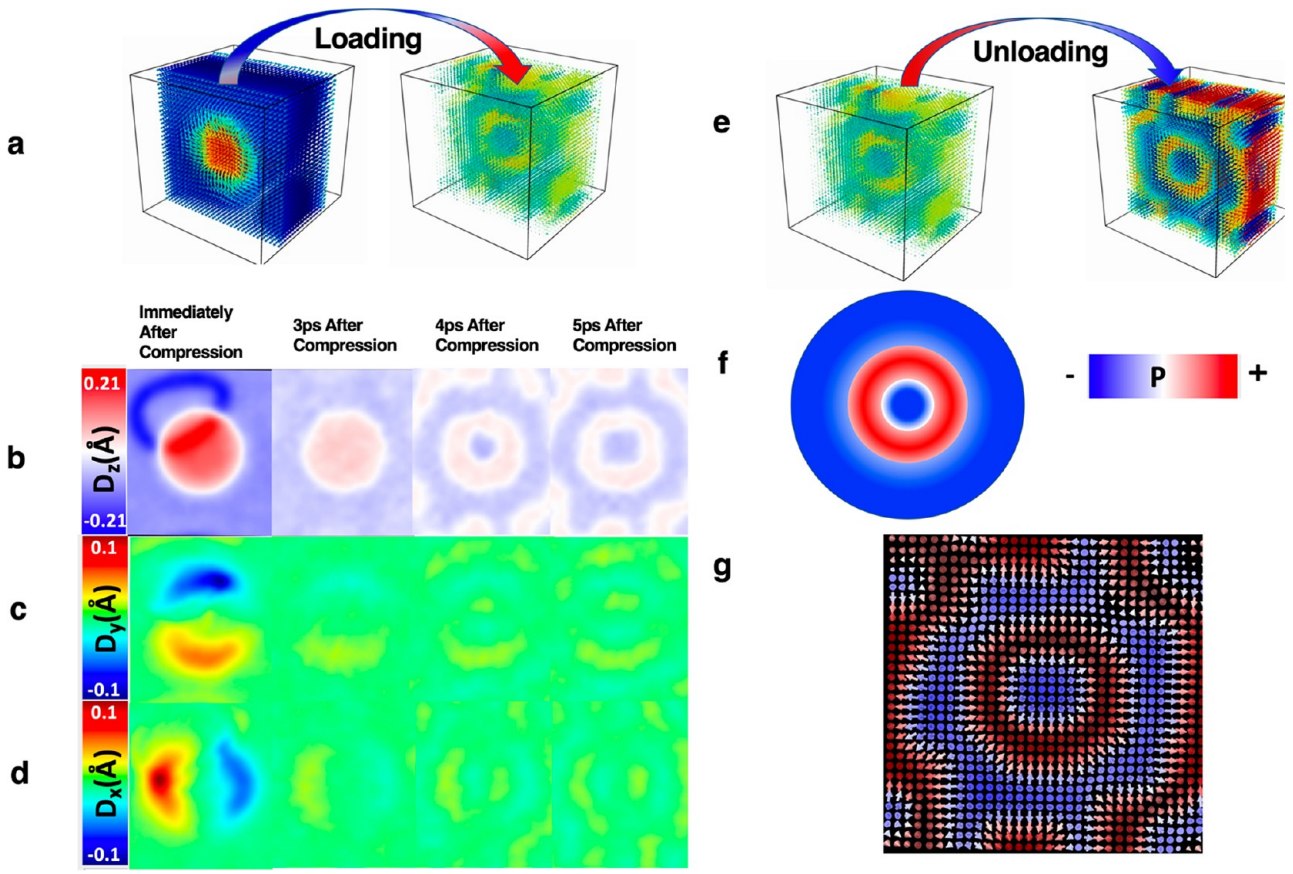

Figure 3. Polarization dynamics under isotropic compression. (a) Snapshots of polarization structure before and after compression. (b) (001) Plane perspective view of unit cells colored by [001] Ti polar displacements after compression. (c,d) (001) Plane perspective slice of unit cells colored by in-plane ([010] and [100]) Ti polar displacements after compression. (e) Snapshots of polarization texture before and after unloading. (f) A schematic of ideal skyrmionium. (g) Skyrmionium formation visualized by Ti displacement vector on each PTO unit cells.

$Pm\bar{3}m$ space group (see Figure S2b). In hydrostatic compression experiments and DFT calculations, multiple pressure-induced phase changes have been suggested for PTO, including the aforementioned $Pm\bar{3}m$ paraelectric phase, as well as rhombohedral R3C, $R\bar{3}C$ phases, and pseudocubic/tetragonal *I*4/*mcm* and *I*4*cm* phases with the latter 4 space groups adopting octahedral rotations.[45−49] Here, we manipulated the *P*4*mm* symmetry of the PTO ground-state structure within the skyrmion superlattice through either breaking the symmetry via uniaxial compression along the polarization axis or preserving the symmetry through isotopically compressing the system. As STO has much higher rigidity than PTO in terms of its elastic constants (both in our model and experimentally, see Supporting Information sections SI and SII), the majority of the compression will occur with the PTO structure.

We first examined the effect of uniaxial compression. The heterostack was loaded at a rate of 1.0% per picosecond (ps) and then relaxed for 12 ps at 10 K. The strain was applied by uniformly scaling the simulation box. Upon compression, we saw an increase in the *ab* polar displacements, which resulted in an increased skyrmion radius. This is illustrated in Figure 2a,b, which shows an (001) plane top slice of the Ti polar displacements at 0% and 1.0% compression along the *c* ([001]). At 2% compression, the *ab* plane polarization of the top of the skyrmion begins to decline (see Figure S3), and we find depolarization at the interface that results in the top plane of the skyrmion being 2 unit cells lower in the PTO layer. In the depolarized unit cells, we see octahedral rotations, which further indicates the formation of a high local pressure, as well as that of a *I*4/*mcm* phase. Conversely, the bulk part of PTO remains unrotated.

The depolarization becomes more prominent as the degree of applied strain increases. This is highlighted in Figure 2c,d, which shows the (010) plane view of the skyrmion texture at 0% and 2.7% compression. We observe a clear "squishing" of the skyrmion because of depolarization at the interface. This was further quantified by examining the magnitude of the Ti polar displacements in the PTO layers as a function of strain, which is plotted in Figure S2. We saw a steady decline in polarization due to the *c* axial compression, with a rapid increase in the rate near ∼2.5% due to depolarization at the interface. Upon compression of up to 3.0%, we saw annihilation of the skyrmion.

To understand the interfacial depolarization and skyrmion annihilation mechanisms, we plotted the average local *c* axis lattice constant as a function of position along the interface direction at 0% strain for reference and at 2.5%, 2.7%, and 3.0% strain just after compression, as shown in Figure 2e. The same local *c* lattice constants were plotted after the system was allowed to evolve and reach a steady state in Figure 2f. As the elastic constant C_{11} of STO is nearly 6 times larger than the elastic constant C_{33} of PTO (both experimentally and within our model; see Supporting Information section SI and SII for details), the change in the local *c* lattice constants is much more compliant to STO, which results in the majority of the

https://doi.org/10.1021/acs.jpclett.2c03029
J. Phys. Chem. Lett. 2022, 13, 11335−11345

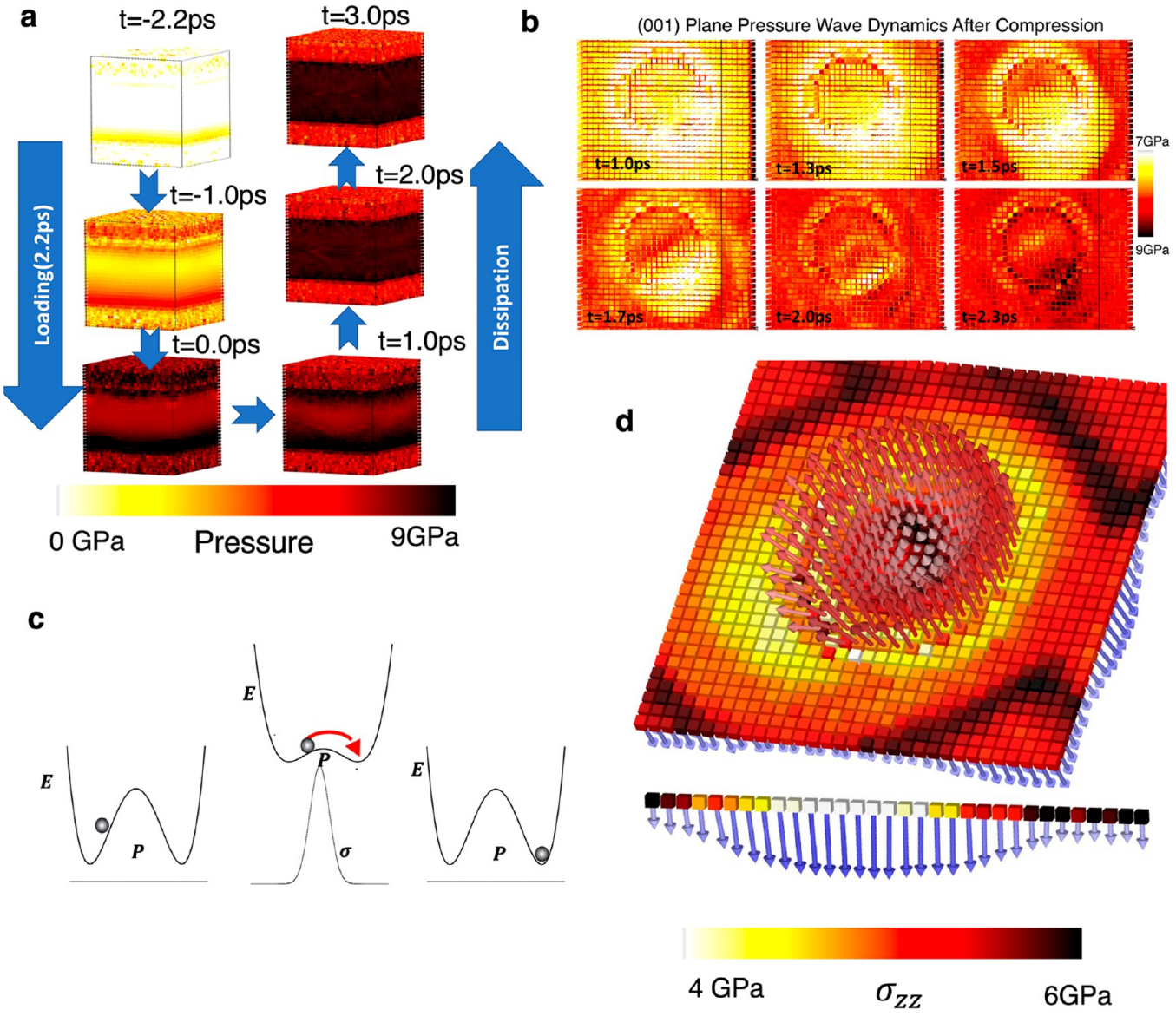

Figure 4. Strain wave dynamics after isotropic compression. (a) Pressure evolution under isotropic loading of the skyrmion system. Isotropic loading results in a high-pressure state with a pressure gradient within the PTO layers. This pressure gradient is slowly dissipated after compression, which results in uniform pressure for the PTO layer and a decline in pressure for the STO layer. (b) During the dissipation process, the local pressure exhibits wavelike dynamics within the middle of the skyrmion in the (001) plane. These wavelike dynamics ultimately result in a reversal of the polarization in some domains. (c) Schematic of strain-wave-induced polarization reversal. (d) Local z strain profiles superimposed with polarization vectors.

compression occurring in the PTO layer. Interestingly, just after compression by 2.5%, 2.7%, and 3.0%, the local strain profiles are very similar to a major decline in the strain gradient, especially within the bulk of the PTO layer. At 2.5% and 2.7% strain, an appreciable strain gradient can be maintained to preserve the skyrmion structure, but with depolarization at the interface where the gradient results in a nonpolar $I4/mcm$ phase for PTO. At 3.0% compression, the PTO region loses its tetragonality, which results in a uniform nonpolar state and the annihilation of the skyrmion structure.

We further understood the depolarization mechanism by comparing the local pressure after compression and relaxation for 2.7% and 3.0% compression. In the two systems, the high-pressure regions developed at the interface in which the 3.0% compression system showed a slight increase in the interfacial pressure. While the 2.7% compression system maintained the interfacial pressure, we observed a rapid release of the accumulated interfacial pressure and resulting complete depolarization of PTO upon 3.0% compression, which indicated the interfacial pressure exceeded a mechanical threshold. Figure 2i,j provides side-by-side snapshots of the evolution of the polarization and the local pressure. A video of the skyrmion annihilation is provided in Supporting Video S3, and its local pressure is shown in Supporting Video S4. Interestingly, the dissipation of the local pressure gradient lags the depolarization front, which indicates this is an inherently dynamic process where complex interactions between polarization and strain fields play a critical role. Our simulation showed a dynamic release of large pressure accumulated at the PTO/STO interface triggering the lattice deformation in the form of octahedral rotations throughout the entirety of PTO, subsequently followed by the rapid depolarization of PTO.

https://doi.org/10.1021/acs.jpclett.2c03029
J. Phys. Chem. Lett. 2022, 13, 11335−11345

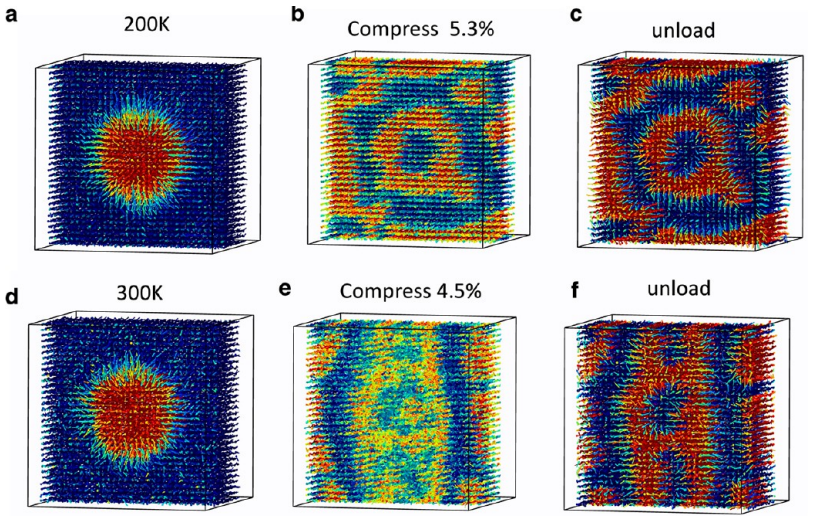

Figure 5. Skyrmionium formation at 200 and 300 K. (a) Snapshots of polarization texture before loading at 200 K. (b) Polarization texture under compression at 200 K. (c) Polarization map after unloading to form skyrmionium structure at 200 K. (d–f) Similar skyrmionium formation seen at 300 K.

We examined the effect of temperature by repeating the simulations at 300 K. The results were somewhat similar, but the critical strain of the annihilation of the skyrmion was decreased to 2.5%. At compression of up to 2.0%, significant depolarization was seen at the interface, and at 2.5%, the skyrmion was annihilated. Videos of the dynamics at 300 K for 2.0% and 2.5% strain are provided in Supporting Videos S5 and S6.

We next examined the dynamics of skyrmions under isotropic compression, which was expected to preserve the tetragonality of the PTO layer under pressure. Again, the strain was applied by uniformly scaling the simulation box. We first compressed each axis by 2.2% over 2.2 ps (*i.e.*, volume compression of 6.5%) at low temperature to isolate the effects of compression from thermal noise. After loading, the system was then relaxed over 15 ps. A video of the dynamics is provided in Supporting Video S7. A snapshot of the skyrmion structure before and 15 ps after loading is provided in Figure 3a. Unlike the uniaxial compression that results in the total depolarization and skyrmion annihilation, the isotropic compression causes reversal of polarization in some regions to create a concentric polar pattern out of the original skyrmion, as illustrated in Figure 3a. Figure 3b provides snapshots of the domain formation process using Ti displacement in the [001] direction. Immediately after compression, the overall [001] polarization gradually reduced before a concentric polarization pattern emerged.

Figure 3c,d demonstrates the substantial loss of the in-plane polarization under the isotropic compression. In addition, the simulation showed the formation of antiphased octahedral rotations throughout the entirety of PTO upon compression, which indicated formation of a tetragonal *I*4/*mcm* phase. This was quantified by computation of the O−O−O bond angle distribution with a cutoff of 3 Å, which defines the TiO_6 octahedra. The global presence of octahedral rotations was signified by significant splitting of the 120° peak, as illustrated in Figure S3.

We next examined the dynamics upon unloading, where we expanded the lattice back to its original lattice constants over 2.2 ps. Upon unloading, the magnitude of [001] polarization increases, and the [010] and [100] polarizations are restored, thereby creating multiple domains with in-plane polarization, including the newly formed concentric pattern shown in Figure 3e. We computed the topological charge density map plotted in Figure S4. Over the concentric polarization pattern, the topological charge density goes from negative to positive and results in a total topological charge of $Q = 0$, which is known as skyrmionium and consists of a pair of skyrmions with opposite topological charge $Q = 1$ and $Q = -1$[32] that reside in a concentric manner. The polarization map of the skyrmionium obtained here (Figure 3g) was found to be remarkably similar to the X-ray map of isolated magnetic skyrmioniums seen in NiFe.[35]

We examined the evolution of the local pressure in the system to understand the mechanism of the skyrmionium formation. Upon loading, we see the formation of a high-pressure gradient within PTO, as illustrated in Figure 4a. Because of the higher rigidity of STO, the gradient is slowly dissipated in the compressed structure, which results in uniform pressure individually within the PTO and STO layers, with STO being of lower pressure. During dissipation, we observed the evolution of pressure waves in the center of the skyrmion structure, as illustrated in Figure 4b. Dissipation of these waves to a uniform pressure state led to polarization reversal, thereby indicating an up-conversion of acoustic waves to optical phonon modes. The polarization response was found to correlate most strongly with the z component of the stress tensor. Two snapshots of the polarization profile overlaid with the local stress are shown in Figure 4d, where in regions of high z stress, the polarization is reduced in comparison with lower stress regions. The flipping of the polarization via these dynamic waves can be understood through the diagram in Figure 4c. If a region in the lattice is driven to a high z stressed state by the dynamic strain propagation, the potential energy for polarization flipping is lowered, which allows individual unit cells to be driven over the barrier. After the wave dissipates and the strain becomes uniform, the flipped polarization of the unit cell will become locked as the original energy barrier is restored.

We examined the robustness of the skyrmion-to-skyrmionium phase transition pathway against strain rate and thermal noise by thermalizing the skyrmion system at 200 and

https://doi.org/10.1021/acs.jpclett.2c03029
J. Phys. Chem. Lett. 2022, 13, 11335−11345

300 K and repeating the isotropic loading and unloading simulation. At 200 K, a skyrmionium transition was observed with a compression of 5.3% by total volume (Figure 5a−c), which is similar to the one observed at 10 K (Figure 3). The dynamics under 300 K are illustrated in Figure 5d−f. Under a loading of 4.5%, we again observed the formation of a similar concentric polarization domain indicative of a skyrmionium transition, which indicated the existence of the skyrmion-to-skyrmionium transition at room temperature.

The effect of strain rate was examined with the system at 200 K and a lower strain rate of 0.1%/ps. We found that the transition threshold was reduced to 4.9%, above which the original skyrmion transformed into fragments of multiple nanodomains upon unloading (see Supporting Information section SV). Whether the skyrmion transforms into a nontrivial polarization pattern or fragmented nanodomains will likely depend on the domain size, strain rate, and percentage. From the well-known Landau−Lifshitz−Kittel scaling laws,[37−39] which dictate the domain size should grow proportionally to the square root of the film thickness, the formation of these new nanodomains on the creation of a thinner STO/PTO film is expected. The consistently seen formation of concentric circular domains can be attributed to the topologically protected nature of a skyrmion and that the concentric circular pattern is a minimal switching pathway to forming more domains within the skyrmion structure.

In conclusion, we have demonstrated the ability to mechanically manipulate polar skyrmions through compressive strain. We found a squishing-to-annihilation transition pathway under uniaxial compression along the *c* polarization axis and a skyrmion-to-skyrmionium transition pathway under isotropic compression. In both strain modes, depolarization occurs when the applied strain becomes too high to maintain the skyrmion structure. Under uniaxial compression, the dissipation of strain gradients results in the total depolarization and formation of a uniform nonpolar *I*4/*mcm* phase in the PTO layers. In contrast, under isotropic compression, the propagation of pressure waves through the system activates optical phonon modes that reverse the polarization inside the skyrmion to form a skyrmionium topological structure. Rapid depolarization of the superlattice under uniaxial compression could be of interest for pulse power generation technologies through the force−electric effect,[30,31] while the increased number of domain walls formed with a local polarization curl in the skyrmionium is anticipated to lead to more areas of local negative permittivity and resulting potential enhancement of the dielectric constant of the superlattice.[7] It should be noted that the high strain rates employed here will be difficult to achieve in a laboratory setting. Since the effects we found are dictated by symmetry, we expect them to persist at lower strain rates, though the required strain requirement will most likely be decreased.

Our results highlight how mechanically manipulating the subtle symmetry of strain and polarization boundary conditions can dynamically invoke different phase changes within these next generation ferroelectric materials and further demonstrate the ability of topological defects formed in ferromagnetic materials to be realizable in ferroelectric materials.[11,12] While, in principle, a well-developed traditional classical force field could potentially investigate the dynamics performed here, we did not find one in the literature that could be easily adapted for this study. Because of the complex orbital hybridization that gives rise to ferroelectricity[50,51] in $PbTiO_3$, it is very difficult to develop a traditional classical force field that well describes both polarization dynamics and mechanical properties. Since we had already developed a neural network force field for $PbTiO_3$,[15] we decided to adapt it for this study rather than try to improve existing classical force fields. Combined with previous studies of light[9,14,15] and electric field[6,7,13] manipulation, the NN/MM simulations performed here provide a promising outlook for broad optical−mechanical−electrical control of polar topologies within the emerging field of ferroelectric "topotronics."[11]

METHODS

QMD Training Data Generation. Ground truth data was generated using density functional theory[52] (DFT)-based QMD simulations using the Vienna Ab inito Software Package (VASP).[53,54] Electronic states were calculated within the projected augmented wavevector method,[55,56] and the Pb $6s^26p^6$, Ti $3s^23p^63d^24s^2$, and O $2s^22p^6$ electronic states were treated explicitly. The training data was generated in the canonical (NVT) ensemble at a temperature of 300 K in PTO's ferroelectric tetragonal structure with multiple densities, tetragonalities, and sheared configurations, as well as at 1200 K (well above the Curie temperature of ∼770 K[57]) to fully explore the potential energy surface. A full description of the training process is provided in Supporting Information section SI. QMD data was generated within the framework of with the meta generalized gradient approximation (GGA) exchange correlation functional, SCAN.[58] SCAN was chosen because it gave good values for the elastic constants without suffering from the problems of supertetragonality seen in GGA-type exchange functionals (see Supporting Information section SI for details).[59] All training data was generated with 4 × 4 × 4 unit cell PTO structures using gamma point sampling of the Brillouin zone. A complete description of the training data generation is described in Supporting Information section SI.

NNQMD Model Development. NNQMD uses a feed-forward neural network architecture consisting of an input layer, multiple hidden layers, and an output layer. Nodes are connected with adjustable weights that are fit to the ground truth QMD training data. The atomic environment is featurized using rotationally, translationally, permutationally, invariant symmetry functions[40,41] with a finite cutoff. Atomic forces are then computed by taking the derivative of the network and symmetry functions with respect to the atomic coordinate. The NNQMD model was trained by included energy, forces, and the stress tensor in the loss function with an adaptive weighting scheme (see Supporting Information section SI for details). After training, the NNQMD model was evaluated in terms of the predicted radial distribution functions, lattice constants, elastic modulus tensor, and bulk modulus. Comparison between the NNQMD and DFT-SCAN radial distribution functions are shown in Figure S1, for which there is excellent agreement. A table comparing the NNQMD computed lattice and elastic constants with the DFT and experiment results are provided in Table S1, which again show good agreement. Full details on model generation, training, and validation are provided in Supporting Information materials section SI. We have uploaded the training data files and neural network parameter binary files to the following Web site: https://zenodo.org/record/7293180. The neural network files can be read by the open source AENET software,[60] which has been implemented into our molecular dynamics code named RXMD.[61]

https://doi.org/10.1021/acs.jpclett.2c03029
J. Phys. Chem. Lett. 2022, 13, 11335−11345

Local Pressure/Stress Computation. The local stress was computed through the elastic approximation using the model elastic modulus tensor C_{ijkl} and computation of local strain ϵ_{kl} from the local lattice constants and angles for each unit cell.

$$\sigma_{ij} = C_{ijkl}\epsilon_{kl}$$

■ ASSOCIATED CONTENT

Supporting Information

The Supporting Information is available free of charge at https://pubs.acs.org/doi/10.1021/acs.jpclett.2c03029.

Videos of polarization dynamics (ZIP)

Additional description of neural network and multiscale simulation methods and additional results, including average polar displacements under *c* axis compression and octahedral rotations under uniaxial compression, temperature and strain rate dependence of skyrmionium phase transition under isotropic compression, dynamics of polar skyrmions under increased isotropic compression, and descriptions of polarization dynamics videos (PDF)

■ AUTHOR INFORMATION

Corresponding Author

Aiichiro Nakano − *Collaboratory for Advanced Computing and Simulations, University of Southern California, Los Angeles, California 90089-0242, United States of America;* orcid.org/0000-0003-3228-3896; Email: anakano@usc.edu

Authors

Thomas Linker − *Collaboratory for Advanced Computing and Simulations, University of Southern California, Los Angeles, California 90089-0242, United States of America*

Ken-ichi Nomura − *Collaboratory for Advanced Computing and Simulations, University of Southern California, Los Angeles, California 90089-0242, United States of America*

Shogo Fukushima − *Department of Physics, Kumamoto University, Kumamoto 860-8555, Japan*

Rajiv K. Kalia − *Collaboratory for Advanced Computing and Simulations, University of Southern California, Los Angeles, California 90089-0242, United States of America*

Aravind Krishnamoorthy − *Collaboratory for Advanced Computing and Simulations, University of Southern California, Los Angeles, California 90089-0242, United States of America;* orcid.org/0000-0001-6778-2471

Kohei Shimamura − *Department of Physics, Kumamoto University, Kumamoto 860-8555, Japan;* orcid.org/0000-0003-3235-2599

Fuyuki Shimojo − *Department of Physics, Kumamoto University, Kumamoto 860-8555, Japan*

Priya Vashishta − *Collaboratory for Advanced Computing and Simulations, University of Southern California, Los Angeles, California 90089-0242, United States of America;* orcid.org/0000-0003-4683-429X

Complete contact information is available at: https://pubs.acs.org/10.1021/acs.jpclett.2c03029

Author Contributions

‖T.L. and K.N. contributed equally to the work. T.L., K.N., R.K.K., A.K., A.N., K.S., F.S., and P.V. designed the work. T.L. generated the first principles QMD training data for the NNQMD model. T.L., K.N., S.F., A.K., A.N., K.S., F.S., and P.V. designed the NNQMD training framework. T.L. trained the NNQMD and MM models. T.L. and K.N. developed the multiscale NN/MM framework and performed the NN/MM simulations. All authors participated in the analysis of the data and writing the manuscript

Notes

The authors declare no competing financial interest.

■ ACKNOWLEDGMENTS

This work was supported as part of the Computational Materials Sciences Program funded by the U.S. Department of Energy, Office of Science, Basic Energy Sciences, under Award Number DE-SC0014607. Simulations were performed at the Argonne Leadership Computing Facility under the DOE INCITE and Aurora Early Science programs and at the Center for Advanced Research Computing of the University of Southern California. T.L was supported by the U.S. Department of Energy, Office of Science, Office of Workforce Development for Teachers and Scientists, Office of Science Graduate Student Research (SCGSR) program. The SCGSR program is administered by the Oak Ridge Institute for Science and Education for the DOE under contract number DE-SC0014664. K.N. was partially supported by an NSF grant, Cyber Training on Materials Genome Innovation for Computational Software (CyberMAGICS), under award number 2118061.

■ REFERENCES

(1) Everschor-Sitte, K.; Masell, J.; Reeve, R. M.; Kläui, M. Perspective: Magnetic Skyrmions—Overview of Recent Progress in an Active Research Field. *J. Appl. Phys.* **2018**, *124* (24), 240901.

(2) Tokura, Y.; Kanazawa, N. Magnetic Skyrmion Materials. *Chem. Rev.* **2021**, *121* (5), 2857−2897.

(3) Göbel, B.; Mertig, I.; Tretiakov, O. A. Beyond Skyrmions: Review and Perspectives of Alternative Magnetic Quasiparticles. *Phys. Rep.* **2021**, *895*, 1−28.

(4) Parkin, S. S. P.; Hayashi, M.; Thomas, L. Magnetic Domain-Wall Racetrack Memory. *Science* **2008**, *320* (5873), 190−194.

(5) Das, S.; Tang, Y. L.; Hong, Z.; Gonçalves, M. A. P.; McCarter, M. R.; Klewe, C.; Nguyen, K. X.; Gómez-Ortiz, F.; Shafer, P.; Arenholz, E.; Stoica, V. A.; Hsu, S. L.; Wang, B.; Ophus, C.; Liu, J. F.; Nelson, C. T.; Saremi, S.; Prasad, B.; Mei, A. B.; Schlom, D. G.; Íñiguez, J.; García-Fernández, P.; Muller, D. A.; Chen, L. Q.; Junquera, J.; Martin, L. W.; Ramesh, R. Observation of Room-Temperature Polar Skyrmions. *Nature* **2019**, *568* (7752), 368−372.

(6) Han, L.; Addiego, C.; Prokhorenko, S.; Wang, M.; Fu, H.; Nahas, Y.; Yan, X.; Cai, S.; Wei, T.; Fang, Y.; Liu, H.; Ji, D.; Guo, W.; Gu, Z.; Yang, Y.; Wang, P.; Bellaiche, L.; Chen, Y.; Wu, D.; Nie, Y.; Pan, X. High-Density Switchable Skyrmion-like Polar Nanodomains Integrated on Silicon. *Nature* **2022**, *603* (7899), 63−67.

(7) Das, S.; Hong, Z.; Stoica, V. A.; Gonçalves, M. A. P.; Shao, Y. T.; Parsonnet, E.; Marksz, E. J.; Saremi, S.; McCarter, M. R.; Reynoso, A.; Long, C. J.; Hagerstrom, A. M.; Meyers, D.; Ravi, V.; Prasad, B.; Zhou, H.; Zhang, Z.; Wen, H.; Gómez-Ortiz, F.; García-Fernández, P.; Bokor, J.; Íñiguez, J.; Freeland, J. W.; Orloff, N. D.; Junquera, J.; Chen, L. Q.; Salahuddin, S.; Muller, D. A.; Martin, L. W.; Ramesh, R. Local Negative Permittivity and Topological Phase Transition in Polar Skyrmions. *Nat. Mater.* **2021**, *20* (2), 194−201.

(8) Hsu, S.-L.; McCarter, M. R.; Dai, C.; Hong, Z.; Chen, L.-Q.; Nelson, C. T.; Martin, L. W.; Ramesh, R. Emergence of the Vortex State in Confined Ferroelectric Heterostructures. *Adv. Mater.* **2019**, *31* (36), 1901014.

(9) Stoica, V. A.; Laanait, N.; Dai, C.; Hong, Z.; Yuan, Y.; Zhang, Z.; Lei, S.; McCarter, M. R.; Yadav, A.; Damodaran, A. R.; Das, S.; Stone, G. A.; Karapetrova, J.; Walko, D. A.; Zhang, X.; Martin, L. W.;

Ramesh, R.; Chen, L. Q.; Wen, H.; Gopalan, V.; Freeland, J. W. Optical Creation of a Supercrystal with Three-Dimensional Nanoscale Periodicity. *Nat. Mater.* **2019**, *18* (4), 377−383.
(10) Du, K.; Zhang, M.; Dai, C.; Zhou, Z. N.; Xie, Y. W.; Ren, Z. H.; Tian, H.; Chen, L. Q.; Van Tendeloo, G.; Zhang, Z. Manipulating Topological Transformations of Polar Structures through Real-Time Observation of the Dynamic Polarization Evolution. *Nat. Commun.* **2019**, *10* (1), 4864.
(11) Tian, G.; Yang, W. D.; Gao, X. S.; Liu, J.-M. Emerging Phenomena from Exotic Ferroelectric Topological States. *APL Mater.* **2021**, *9* (2), 020907.
(12) Seidel, J. Nanoelectronics Based on Topological Structures. *Nat. Mater.* **2019**, *18* (3), 188−190.
(13) Behera, P.; May, M. A.; Gomez-Ortiz, F.; Susarla, S.; Das, S.; Nelson, C. T.; Caretta, L.; Hsu, S.-L.; McCarter, M. R.; Savitzky, B. H.; Barnard, E. S.; Raja, A.; Hong, Z.; Garcia-Fernandez, P.; Lovesey, S. W.; van der Laan, G.; Ercius, P.; Ophus, C.; Martin, L. W.; Junquera, J.; Raschke, M. B.; Ramesh, R. Electric Field Control of Chirality. *Sci. Adv.* **2022**, *8* (1), eabj8030.
(14) Ahn, Y.; Park, J.; Pateras, A.; Rich, M. B.; Zhang, Q.; Chen, P.; Yusuf, M. H.; Wen, H.; Dawber, M.; Evans, P. G. Photoinduced Domain Pattern Transformation in Ferroelectric-Dielectric Superlattices. *Phys. Rev. Lett.* **2017**, *119* (5), 57601.
(15) Linker, T.; Nomura, K.; Aditya, A.; Fukshima, S.; Kalia, R.; Krishnamoorthy, A.; Nakano, A.; Rajak, P.; Shimmura, K.; Shimojo, F.; Vashishta, P. Exploring Far-from-Equilibrium Ultrafast Polarization Control in Ferroelectric Oxides with Excited-State Neural Network Quantum Molecular Dynamics. *Sci. Adv.* **2022**, *8* (12), eabk2625.
(16) Lu, H.; Bark, C. W.; Esque De Los Ojos, D.; Alcala, J.; Eom, C. B.; Catalan, G.; Gruverman, A. Mechanical Writing of Ferroelectric Polarization. *Science* **2012**, *336* (6077), 59−61.
(17) Tang, Y.; Zhu, Y.; Wu, B.; Wang, Y.; Yang, L.; Feng, Y.; Zou, M.; Geng, W.; Ma, X. Periodic Polarization Waves in a Strained, Highly Polar Ultrathin $SrTiO_3$. *Nano Lett.* **2021**, *21* (14), 6274−6281.
(18) Kim, K.-E.; Jeong, S.; Chu, K.; Lee, J. H.; Kim, G.-Y.; Xue, F.; Koo, T. Y.; Chen, L.-Q.; Choi, S.-Y.; Ramesh, R.; Yang, C.-H. Configurable Topological Textures in Strain Graded Ferroelectric Nanoplates. *Nat. Commun.* **2018**, *9* (1), 403.
(19) Wang, Y. J.; Feng, Y. P.; Zhu, Y. L.; Tang, Y. L.; Yang, L. X.; Zou, M. J.; Geng, W. R.; Han, M. J.; Guo, X. W.; Wu, B.; Ma, X. L. Polar Meron Lattice in Strained Oxide Ferroelectrics. *Nat. Mater.* **2020**, *19*, 881−886.
(20) Shao, Y.-T.; Das, S.; Hong, Z.; Xu, R.; Chandrika, S.; Gómez-Ortiz, F.; García-Fernández, P.; Chen, L.-Q.; Hwang, H.; Junquera, J.; Martin, L.; Ramesh, R.; Muller, D. Emergent Chirality in a Polar Meron to Skyrmion Transition Revealed by 4D-STEM. *Microsc. Microanal.* **2021**, *27* (S1), 348−350.
(21) Zubko, P.; Catalan, G.; Tagantsev, A. K. Flexoelectric Effect in Solids. *Annu. Rev. Mater. Res.* **2013**, *43* (1), 387−421.
(22) Wang, B.; Gu, Y.; Zhang, S.; Chen, L.-Q. Flexoelectricity in Solids: Progress, Challenges, and Perspectives. *Prog. Mater. Sci.* **2019**, *106*, 100570.
(23) Behler, J. Perspective: Machine Learning Potentials for Atomistic Simulations. *J. Chem. Phys.* **2016**, *145* (17), 170901.
(24) Karniadakis, G. E.; Kevrekidis, I. G.; Lu, L.; Perdikaris, P.; Wang, S.; Yang, L. Physics-Informed Machine Learning. *Nat. Rev. Phys.* **2021**, *3* (6), 422−440.
(25) Warshel, A.; Levitt, M. Theoretical Studies of Enzymic Reactions: Dielectric, Electrostatic and Steric Stabilization of the Carbonium Ion in the Reaction of Lysozyme. *J. Mol. Biol.* **1976**, *103* (2), 227−249.
(26) Warshel, A. Multiscale Modeling of Biological Functions: From Enzymes to Molecular Machines (Nobel Lecture. *Angew. Chemie Int. Ed.* **2014**, *53* (38), 10020−10031.
(27) Shimamura, K.; Fukushima, S.; Koura, A.; Shimojo, F.; Misawa, M.; Kalia, R. K.; Nakano, A.; Vashishta, P.; Matsubara, T.; Tanaka, S. Guidelines for Creating Artificial Neural Network Empirical Interatomic Potential from First-Principles Molecular Dynamics Data under Specific Conditions and Its Application to α-Ag_2Se. *J. Chem. Phys.* **2019**, *151* (12), 124303.
(28) Krishnamoorthy, A.; Nomura, K.; Baradwaj, N.; Shimamura, K.; Rajak, P.; Mishra, A.; Fukushima, S.; Shimojo, F.; Kalia, R.; Nakano, A.; Vashishta, P. Dielectric Constant of Liquid Water Determined with Neural Network Quantum Molecular Dynamics. *Phys. Rev. Lett.* **2021**, *126* (21), 216403.
(29) Rajak, P.; Baradwaj, N.; Nomura, K.; Krishnamoorthy, A.; Rino, J. P.; Shimamura, K.; Fukushima, S.; Shimojo, F.; Kalia, R.; Nakano, A.; Vashishta, P. Neural Network Quantum Molecular Dynamics, Intermediate Range Order in $GeSe_2$, and Neutron Scattering Experiments. *J. Phys. Chem. Lett.* **2021**, *12* (25), 6020−6028.
(30) Shkuratov, S. I.; Baird, J.; Antipov, V. G.; Talantsev, E. F.; Chase, J. B.; Hackenberger, W.; Luo, J.; Jo, H. R.; Lynch, C. S. Ultrahigh Energy Density Harvested from Domain-Engineered Relaxor Ferroelectric Single Crystals under High Strain Rate Loading. *Sci. Rep.* **2017**, *7* (1), 46758.
(31) Gao, Z.; Peng, W.; Chen, B.; Redfern, S. A. T.; Wang, K.; Chu, B.; He, Q.; Sun, Y.; Chen, X.; Nie, H.; Deng, W.; Zhang, L.; He, H.; Wang, G.; Dong, X. Giant Power Output in Lead-Free Ferroelectrics by Shock-Induced Phase Transition. *Phys. Rev. Mater.* **2019**, *3* (3), 35401.
(32) Zhang, X.; Xia, J.; Zhou, Y.; Wang, D.; Liu, X.; Zhao, W.; Ezawa, M. Control and Manipulation of a Magnetic Skyrmionium in Nanostructures. *Phys. Rev. B* **2016**, *94* (9), 94420.
(33) Wang, J.; Xia, J.; Zhang, X.; Zheng, X.; Li, G.; Chen, L.; Zhou, Y.; Wu, J.; Yin, H.; Chantrell, R.; Xu, Y. Magnetic Skyrmionium Diode with a Magnetic Anisotropy Voltage Gating. *Appl. Phys. Lett.* **2020**, *117* (20), 202401.
(34) Kolesnikov, A. G.; Stebliy, M. E.; Samardak, A. S.; Ognev, A. V. Skyrmionium − High Velocity without the Skyrmion Hall Effect. *Sci. Rep.* **2018**, *8* (1), 16966.
(35) Zhang, S.; Kronast, F.; van der Laan, G.; Hesjedal, T. Real-Space Observation of Skyrmionium in a Ferromagnet-Magnetic Topological Insulator Heterostructure. *Nano Lett.* **2018**, *18* (2), 1057−1063.
(36) Yang, J.; Park, H.-K.; Park, G.; Abert, C.; Suess, D.; Kim, S.-K. Robust Formation of Skyrmion and Skyrmionium in Magnetic Hemispherical Shells and Their Dynamic Switching. *Phys. Rev. B* **2021**, *104* (13), 134427.
(37) Landau, L.; Lifshitz, E. On the theory of the dispersion of magnetic permeability in ferromagnetic bodies. *Physikalische Zeitschrift der Sowjetunion* **1935**, *8* (2), 153.
(38) Kittel, C. Theory of the Structure of Ferromagnetic Domains in Films and Small Particles. *Phys. Rev.* **1946**, *70* (11−12), 965−971.
(39) Catalan, G.; Béa, H.; Fusil, S.; Bibes, M.; Paruch, P.; Barthélémy, A.; Scott, J. F. Fractal Dimension and Size Scaling of Domains in Thin Films of Multiferroic $BiFeO_3$. *Phys. Rev. Lett.* **2008**, *100* (2), 27602.
(40) Behler, J.; Lorenz, S.; Reuter, K. Representing Molecule-Surface Interactions with Symmetry-Adapted Neural Networks. *J. Chem. Phys.* **2007**, *127* (1), 014705.
(41) Behler, J.; Parrinello, M. Generalized Neural-Network Representation of High-Dimensional Potential-Energy Surfaces. *Phys. Rev. Lett.* **2007**, *98* (14), 146401.
(42) Shimojo, F.; Hattori, S.; Kalia, R. K.; Kunaseth, M.; Mou, W.; Nakano, A.; Nomura, K. I.; Ohmura, S.; Rajak, P.; Shimamura, K.; Vashishta, P. A Divide-Conquer-Recombine Algorithmic Paradigm for Large Spatiotemporal Quantum Molecular Dynamics Simulations. *J. Chem. Phys.* **2014**, *140* (18), 18A529.
(43) Lier, B.; Poliak, P.; Marquetand, P.; Westermayr, J.; Oostenbrink, C. BuRNN: Buffer Region Neural Network Approach for Polarizable-Embedding Neural Network/Molecular Mechanics Simulations. *J. Phys. Chem. Lett.* **2022**, *13* (17), 3812−3818.
(44) Berg, B.; Lüscher, M. Definition and Statistical Distributions of a Topological Number in the Lattice O(3) σ-Model. *Nucl. Phys. B* **1981**, *190* (2), 412−424.
(45) Jabarov, S. G.; Kozlenko, D. P.; Kichanov, S. E.; Belushkin, A. V.; Savenko, B. N.; Mextieva, R. Z.; Lathe, C. High-Pressure Effect on

the Ferroelectric-Paraelectric Transition in $PbTiO_3$. *Phys. Solid State* **2011**, *53* (11), 2300−2304.
(46) Sani, A.; Hanfland, M.; Levy, D. Pressure and Temperature Dependence of the Ferroelectric−Paraelectric Phase Transition in $PbTiO_3$. *J. Solid State Chem.* **2002**, *167* (2), 446−452.
(47) Frantti, J.; Fujioka, Y.; Nieminen, R. M. Pressure-Induced Phase Transitions in PbTiO3: A Query for the Polarization Rotation Theory. *J. Phys. Chem. B* **2007**, *111* (17), 4287−4290.
(48) Janolin, P.-E.; Bouvier, P.; Kreisel, J.; Thomas, P. A.; Kornev, I. A.; Bellaiche, L.; Crichton, W.; Hanfland, M.; Dkhil, B. High-Pressure Effect on $PbTiO_3$: An Investigation by Raman and X-Ray Scattering up to 63 GPa. *Phys. Rev. Lett.* **2008**, *101* (23), 237601.
(49) Frantti, J.; Fujioka, Y.; Molaison, J. J.; Boehler, R.; Haberl, B.; Tulk, C. A.; dos Santos, A. M. Compression Mechanisms of Ferroelectric $PbTiO_3$ via High Pressure Neutron Scattering. *J. Phys.: Condens. Matter* **2018**, *30* (43), 435702.
(50) Cohen, R. E.; Krakauer, H. Electronic Structure Studies of the Differences in Ferroelectric Behavior of $BaTiO_3$ and $PbTiO_3$. *Ferroelectrics* **1992**, *136* (1), 65−83.
(51) Turik, A. V.; Khasabov, A. G. On the Origin of Ferroelectricity in $PbTiO_3$. *Ferroelectrics* **2000**, *237* (1), 65−71.
(52) Kohn, W.; Sham, L. J. Self-Consistent Equations Including Exchange and Correlation Effects. *Phys. Rev.* **1965**, *140* (4A), A1133−A1138.
(53) Kresse, G.; Hafner, J. Ab Initio Molecular Dynamics for Liquid Metals. *Phys. Rev. B* **1993**, *47* (1), 558−561.
(54) Kresse, G.; Furthmüller, J. Efficient Iterative Schemes for Ab Initio Total-Energy Calculations Using a Plane-Wave Basis Set. *Phys. Rev. B* **1996**, *54* (16), 11169−11186.
(55) Blöchl, P. E. Projector Augmented-Wave Method. *Phys. Rev. B* **1994**, *50* (24), 17953−17979.
(56) Kresse, G.; Joubert, D. From Ultrasoft Pseudopotentials to the Projector Augmented-Wave Method. *Phys. Rev. B* **1999**, *59* (3), 1758−1775.
(57) Jiao, Y.-C.; Li, M.; Qu, B.-Y.; Wu, M.-Y.; Zhang, N.; Guo, P.; Wang, J.-J. First-Principles Study of the Negative Thermal Expansion of PbTiO3. *Comput. Mater. Sci.* **2016**, *124*, 92−97.
(58) Sun, J.; Ruzsinszky, A.; Perdew, J. P. Strongly Constrained and Appropriately Normed Semilocal Density Functional. *Phys. Rev. Lett.* **2015**, *115* (3), 36402.
(59) Zhang, Y.; Sun, J.; Perdew, J. P.; Wu, X. Comparative First-Principles Studies of Prototypical Ferroelectric Materials by LDA, GGA, and SCAN Meta-GGA. *Phys. Rev. B* **2017**, *96* (3), 35143.
(60) Artrith, N.; Urban, A. An Implementation of Artificial Neural-Network Potentials for Atomistic Materials Simulations: Performance for TiO2. *Comput. Mater. Sci.* **2016**, *114*, 135−150.
(61) Nomura, K.; Kalia, R. K.; Nakano, A.; Rajak, P.; Vashishta, P. RXMD: A Scalable Reactive Molecular Dynamics Simulator for Optimized Time-to-Solution. *SoftwareX* **2020**, *11*, 100389.

https://doi.org/10.1021/acs.jpclett.2c03029
J. Phys. Chem. Lett. 2022, 13, 11335−11345